Journal of
Manufacturing and Materials Processing

MDPI

Article

Effect of Load Vector Orientation on Uniaxial Compressive Strength of 3D Photoresin

Evgenii Kozhevnikov [1,*], Mikhail Turbakov [1], Evgenii Riabokon [1,2], Zakhar Ivanov [1], Andrei Golosov [3], Arina Panteleeva [1] and Yan Savitsky [1]

[1] Laboratory of Natural Gas Hydrates, Perm National Research Polytechnic University, Perm 614990, Russia; msturbakov@gmail.com (M.T.); riabokon@pstu.ru (E.R.); zakhar.ivanov.2013@gmail.com (Z.I.); rinapan01@mail.ru (A.P.); yansavitsky@pstu.ru (Y.S.)
[2] State Key Laboratory of Intelligent Construction and Healthy Operation and Maintenance of Deep Underground Engineering, China University of Mining and Technologies, Xuzhou 221116, China
[3] Research and Educational Center for Geomechanics and Geodynamics of Highly Compressed Rocks and Rock Masses, Far Eastern Federal University, Vladivostok 690041, Russia; golosov.am@dvfu.ru
* Correspondence: kozhevnikov_evg@mail.ru

Abstract: Rapid prototyping has a wide range of applications across various fields, both in industry and for private use. It enables the production of individual parts in a short time, independent of supply chains, which is particularly important in remote locations. Among all 3D printing technologies, stereolithography using photo resins is the most accessible and offers the highest printing quality. However, the strength properties of parts made from photo resins remain a critical concern. In this study, we conducted experimental research to investigate the effect of load vector orientation under uniaxial compression on the elastic and mechanical properties of 3D-printed cylindrical samples. The results revealed that samples with layers oriented at 60° to the load vector exhibited the highest strength, while those with layers at 30° to the load vector showed the lowest strength. Samples with layers aligned parallel or perpendicular to the load vector demonstrated similar strength properties. Under quasi-elastic loading, samples with layers parallel to the load vector exhibited the highest Young's modulus and the lowest Poisson's ratio. Conversely, samples with layers oriented at 30° to the load vector displayed the highest Poisson's ratio. Microstructural analysis revealed that the anisotropy in the mechanical properties of the 3D-printed samples is attributed to the layered, heterogeneous structure of the photoresin, which exhibits varying degrees of polymerization along the printing axes. The upper part of each layer, with a lower degree of polymerization, contributes to the ductile behavior of the samples under shear stresses. In contrast, the lower part of the layer, with a higher degree of polymerization, leads to brittle behavior in the samples.

Keywords: stereolithography; 3D printing; uniaxial compression; Young's modulus

Academic Editor: Shuo Yin

Received: 11 December 2024
Revised: 8 January 2025
Accepted: 13 January 2025
Published: 14 January 2025

Citation: Kozhevnikov, E.; Turbakov, M.; Riabokon, E.; Ivanov, Z.; Golosov, A.; Panteleeva, A.; Savitsky, Y. Effect of Load Vector Orientation on Uniaxial Compressive Strength of 3D Photoresin. *J. Manuf. Mater. Process.* **2025**, *9*, 23. https://doi.org/10.3390/jmmp9010023

1. Introduction

Rapid prototyping finds widespread applications across diverse fields [1–3]. The choice of printing technology depends on the intended purpose and the material required [4,5]. Stereolithography (SLA) technology currently boasts the highest print quality and finds utility beyond practical applications, extending to research purposes. The main parameters of parts manufactured using rapid prototyping, in addition to accuracy, are longevity, wear resistance, and strength under mechanical loading. These properties are influenced by the type of material, printing conditions [6–8], and post-processing techniques [9,10]. However, all else being equal, a defining characteristic of SLA printing is the

layer-by-layer heterogeneity of the resulting parts [11,12]. During SLA printing, a part is formed through the layer-wise curing of the material. This process can lead to variations in the strength characteristics of the final part, depending on the angle of the applied load relative to the plane of the layers. This variability arises from the heterogeneity inherent in each layer and the presence of inter-layer contact points. Consequently, parts subjected to loads applied in different directions may exhibit differing levels of resistance and elasticity due to the layered structure. When simulating deformation processes of 3D-printed parts, it is crucial to consider the direction of the load in relation to the orientation of the printed layers to optimize model creation and predict performance accurately.

Numerous studies have investigated the impact of SLA printing angle on the mechanical properties of fabricated parts. Li and Teng [13] explored the influence of layer orientation angle on the tensile strength of SLA samples. Their study employed the following printing parameters: a laser spot diameter of 0.2 mm, a layer thickness of 0.15 mm, and an irradiation speed of 10 m/s. The results indicated that under uniaxial tensile loading, dogbone specimens with printing layers perpendicular to the load exhibited lower elasticity and strength compared to samples oriented parallel to the printing layers. While fracture occurred near the middle of the specimens without noticeable variations, the semi-cylindrical samples with pre-existing cracks displayed the highest strength when printed with inclined layers at 30–45 degrees. Conversely, samples with parallel (0 degrees) and perpendicular (90 degrees) layers exhibited the lowest strength. Furthermore, in specimens with inclined layers, crack growth deviated slightly from the initial pre-crack direction. Li and Teng attributed this phenomenon to weaker bonding between the layers, suggesting that the angle of the layers influences the cohesive strength of the material.

Monzón et al. [14] investigated the effect of the SLA printing angle on the strength properties of samples under flexural loading. The load was applied parallel and perpendicular to the printing layers. In samples where the load is perpendicular to the printing layers, the flexural modulus is higher. With this direction of the flexural loading, tensile stress arises in the sample parallel to the printing layers, which indicates high strength of the layers and weak connection between the layers.

Saini et al. [15] investigated the effect of the printing angle on the compression and tension strength. Stronger samples had the following properties: under tension—along the layers, under compression and flexural loading—with an angle of the layers of 67.5°, under flexural loading with a pre-crack—perpendicular to the layers. It was found that when bending, the less durable samples were those in which the tensile stress acts along the layers or is slightly deviated up to 22.5°, whereas under pure tension these samples are stronger. This suggests that uneven application of stress contributes to a decrease in the strength of printed samples.

Farkas et al. [16] investigated the effect of the printing angle on compression and tension strength. When compressed perpendicular to the layers, the strength of the samples is higher. It is assumed that in samples with a longitudinal arrangement of layers, the presence of defects due to sagging during printing reduces the strength of the parts, and their strength is lower.

Kessler et al. [17] experimentally established that samples in which the tensile stress during bending is parallel to the layers have greater flexural strength. The authors point out that the strength is affected by the presence of defects in the parts, which are formed due to printing features—uneven edges, air bubbles, and foreign inclusions.

While the above-mentioned works state that the samples have greater strength along the printing layers, other studies [6,7,10,18,19] have experimentally established that the strength of samples with layers oriented parallel to the tensile load is lower than that of samples with a perpendicular direction. The authors of Ref. [7] indicate that the reason for

the different strength of the samples is the different direction of laser movement during curing. Cosmi and Dal Maso [18] experimentally established that the Young's modulus is the highest in SLA-printed samples with a tensile load directed perpendicular to the layers, but the strength and deformation are higher in samples with an angular direction. Pandzic [19] investigated the effect of the thickness and orientation of SLA sample layers relative to the load on the tensile strength, and established that the thinner the layers, the higher the strength and elasticity. In samples with layers perpendicular to the load, the Young's modulus is slightly higher, but the strength is noticeably lower at any layer thickness. Reducing the layer thickness in the direction perpendicular to the load makes the material more brittle, resulting in increased rigidity and decreased strength.

Despite extensive research on the influence of layer orientation on the strength properties of 3D-printed parts, a significant gap exists in the literature. Most studies focus primarily on tensile strength, with limited investigation into compressive strength, despite the frequent use of 3D-printed components under compressive loading conditions. Furthermore, experimental results regarding the impact of layer orientation on strength are inconsistent. Some studies report increased strength when the tensile force aligns with the printing direction, while others observe the opposite effect. This lack of consistency hinders a definitive understanding of the underlying failure mechanism and the factors contributing to strength variations with respect to printing layer direction. Additionally, the crucial aspect of sample preparation, particularly for uniaxial compression testing, is often overlooked. As highlighted in Ref. [16], sample sagging can significantly impact layer uniformity and thus test results. Moreover, the use of unsupported printing or printing directly on a moving plate, practices found in some studies, further compromises the reliability of the results.

This research aims to address these knowledge gaps by investigating the influence of 3D printing layer orientation on the compressive strength. This study seeks to elucidate the failure mechanism and identify the reasons for strength variations between samples with different layer orientations. To ensure rigorous and reliable findings, this research incorporates proper sample preparation techniques.

2. Materials and Methods

The samples were manufactured in several stages:

1. Creating digital cylindrical models in CAD KOMPAS 3D software;
2. Pre-printing preparation of digital models in slicer software, installation of supports (Figure 1);
3. Printing samples;
4. Post-printing cleaning of samples from resin and support residues;
5. Post-processing of samples in accordance with the ASTM D7012-23 standard.

Digital cylindrical models were created in CAD software. The sizes of the samples were set in accordance with the ASTM D7012-23 standard, with a length-to-diameter ratio of 2/1, 70 mm in length, and 35 mm in diameter. The digital model was exported to STL format for pre-print. In the slicer software, the samples were placed on the work table, which imitates the moving platform of a 3D printer. The samples were placed on the table with different layer angles (Figure 1), with 3 samples for each printing angle. The angles of 0° (a), 30° (b), 60° (c), and 90° (d) shown in Figure 1 are the angles between the plane of the layer and the axis of the cylindrical sample. The platform with the square grid is the movable plate to which the samples are attached during printing. Samples with angles of 0° (a), 30° (b), and 60° (c) were printed on supports, as shown in the photo. All samples have an orientation relative to the Y-axis (Figure 1). The sample with the layer orientation of 90° (Figure 1d) was printed without supports, directly on the moving plate.

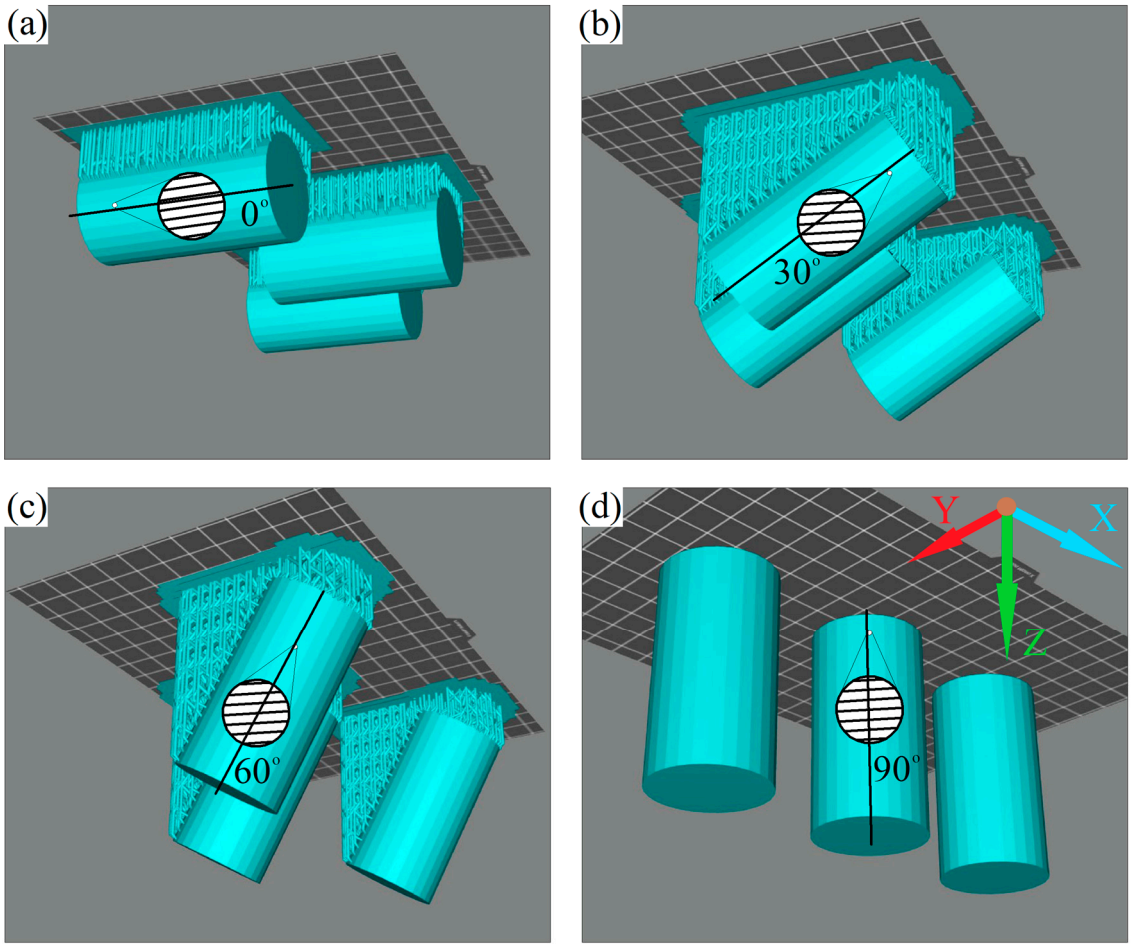

Figure 1. Pre-printing of digital models in the slicer software. Samples are arranged with different layer printing angles: (**a**)—0°; (**b**)—30°; (**c**)—60°; (**d**)—90°. The black line is the axis of the cylindrical sample. The circles show the direction of the printed layers.

The samples were printed on an Anycubic Photon Mono X (Shenzhen Anycubic Technology Co., Ltd., Shenzhen, China) printer using the LCD method, which is the cheapest and most accessible type of SLA printing, and is not inferior in print quality. Due to mask irradiation through the LCD screen, this technology allows for simultaneous irradiation of the entire layer over the area. The printing parameters used in the work are listed in Table 1. The exposure time was determined during preliminary tests and is sufficient to ensure high quality and at the same time reduce the printing time. The layer thickness is set by default, and is 50 μm for Anycubic Photon Mono X. Commercial resin Anycubic Basic Resin Black was used for printing; the color black was chosen to minimize the effect of unwanted light scattering on print quality.

Table 1. Printing parameters.

Parameter	Value
Platform lifting distance	5 mm
Platform lifting speed	3 mm/s
Platform retract speed	3 mm/s
Layer thickness	50 μm
UV power	100%
Normal exposure time	2 s

After printing, supports were removed, and resin residues were washed away using isopropyl alcohol in an ultrasonic bath. Cylindrical samples with an approximate diameter of 35 mm and a length of 70 mm were obtained. Figure 2 depicts the appearance of these samples. Visual inspection of the printing quality revealed that samples printed with parallel (Figure 2a) and inclined layers (Figure 2b,c) exhibited irregular cylindrical shapes due to layer sagging during printing. The ends of these cylinders (Figure 2a–c) displayed non-parallel surfaces, protrusions, irregularities, and residual pimples from support removal. Additionally, defects were observed on the side surfaces, arising from support removal. Further defects related to printing omissions were noted (Figure 2c).

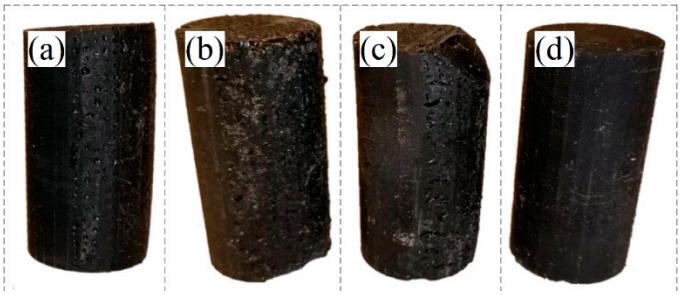

Figure 2. Samples printed with different layer angles—0° (**a**), 30° (**b**), 60° (**c**), and 90° (**d**).

Only samples with vertical layering exhibited an ideal cylindrical shape, fulfilling the requirements outlined in ASTM D7012-23 for uniaxial compression test specimens. While these samples were printed without support structures and incorporated several starting layers with increased strength, this variation is not expected to significantly impact the results of uniaxial compression testing.

The printed samples (Figure 2) were post-processed to a cylindrical shape using a lathe. The turning process and the finished samples are shown in Figure 3. The samples were initially designed to be slightly larger in size in order to bring them to an ideal cylindrical shape. The final samples (Figure 3c), ready for uniaxial compression, have a correct cylindrical shape with parallel edges. The size of the samples was 29 mm in diameter and 58 mm in length, which complies with the ASTM D7012-23 standard. The samples were not subjected to the post-curing procedure. Before testing and during post-processing, the samples were stored in a dark place to minimize exposure to natural light. The storage temperature and humidity correspond to normal room conditions. About 2 weeks passed between printing the samples and mechanical testing, which is due to the workload of the apparatus for mechanical testing. Thus, all samples were in the same conditions, and the storage conditions should not affect the results. The influence of the postcuring process on mechanical properties was not the aim of this work, although such an influence should certainly exist [10,19,20].

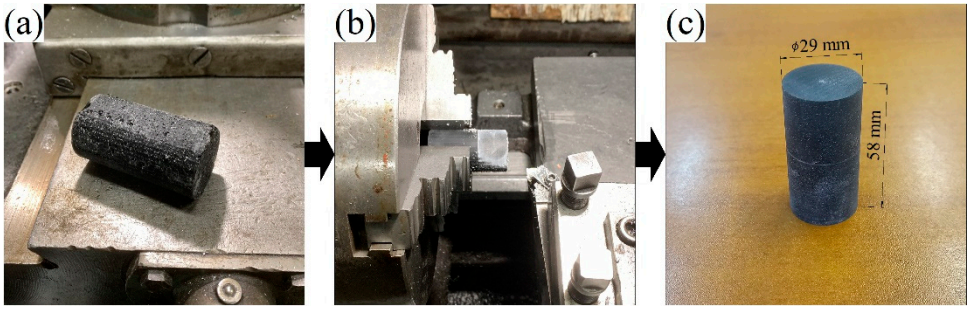

Figure 3. Post-processing of samples: (**a**)—sample before; (**b**)—in process; (**c**)—finished sample.

The mechanical test for uniaxial compression of the samples was carried out using the Rock Mechanics Test System 816 (Figure 4). Figure 4a shows a sample with two pairs of strain gauges glued to the side surface of the sample in the perpendicular direction. The layout of the strain gauges relative to the axes of the printer and the printed layers is shown in Figure 4b. The samples were loaded until complete failure. Additionally, an acoustic emission (AE) sensor was fixed in the middle of the side surface of the sample using a rubber belt.

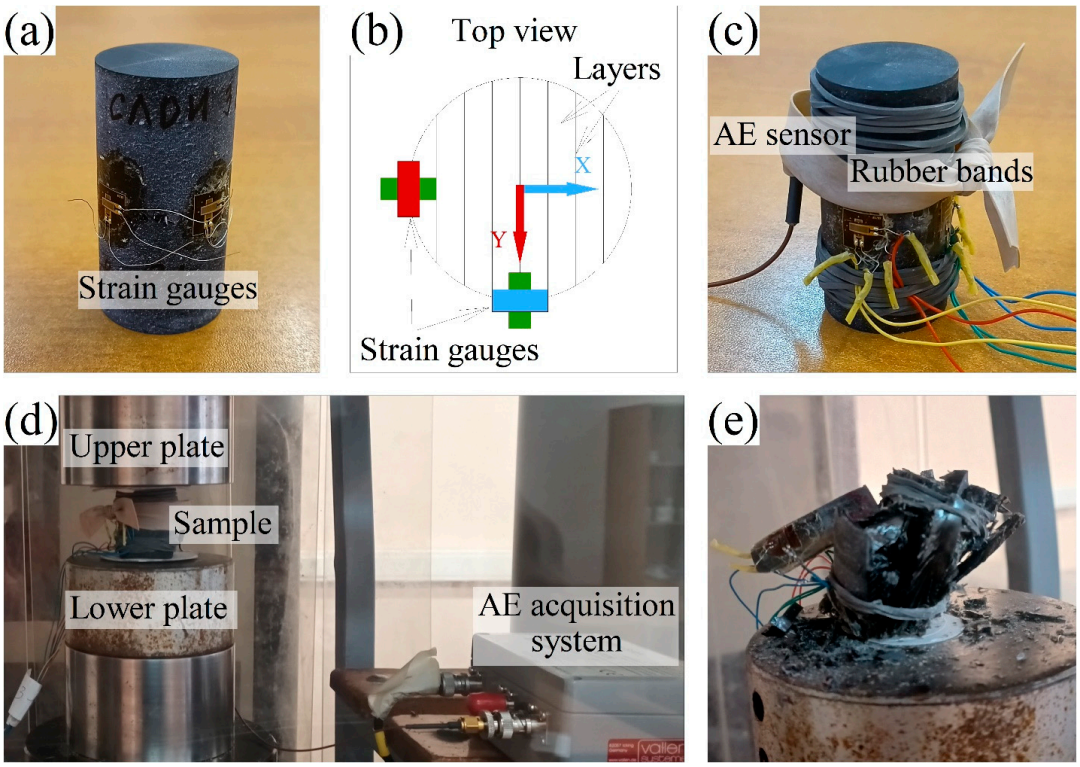

Figure 4. (**a**)—sample with glued strain gauges; (**b**)—diagram of the strain gauge arrangement relative to the layer orientation during printing. The color of the gauges corresponds to the direction of the printing axis along which the strain is measured (see Figure 1); (**c**)—sample with AE sensor ready for testing; (**d**)—sample in the load cell during testing; (**e**)—destroyed sample.

During loading, data from load cells, displacement sensors, and the AE signal recording system (Figure 4d) were recorded on a computer. Uniaxial compression was performed until the specimen failed (Figure 4e). The loading rate for all specimens was 0.1 MPa/s according to the ASTM D7012-23 standard. The stress (P) was calculated using the formula:

$$P = \frac{F}{S} \tag{1}$$

where F is the load (N), and S is the cross-sectional area of the samples (m^2).

Axial deformation was calculated using the formula:

$$\varepsilon_a = \frac{\Delta L}{L} \tag{2}$$

where ΔL is the displacement of the press plate under loading (mm), and L is the length of the sample (mm).

The radial deformation was calculated using the formula:

$$\varepsilon_r = \frac{\Delta d}{d} \tag{3}$$

where Δd is the change in diameter under loading (mm), and d is the diameter of the sample (mm).

Since the sample is very plastic and splits into plates under large axial deformations, the radial and axial deformations were measured by strain gauges only for the elastic deformation zone to calculate the Poisson ratio. For deformations above the quasi-elastic zone, the data from the gauges do not reflect the actual deformation. For the quasi-elastic zone, the Poisson ratio was calculated using the formula:

$$\mu = \frac{\varepsilon_r}{\varepsilon_a} \quad (4)$$

The total axial strain for stress–strain curves is taken from the displacement data of the top plate of the load cell.

3. Results and Discussion

Based on the results of uniaxial compression tests, the strain–stress curves and the total AE signal curve were constructed (Figure 5). The load and deformation measurements during testing begin with preloading with a stress value of up to 20 MPa (Figure 5); this is due to the limitations of the load cell, which has a large error at low loads, since it is designed for high loads at which the sample is destroyed. Nevertheless, with such a preload value, it was possible to obtain a quasi-elastic zone, which is confirmed by the absence of AE signals at stresses of up to 40 MPa (Figure 5). A curve typical for all samples is shown in Figure 5. The strain–stress curve of the samples shows elastic-viscoplastic properties. In the initial period of loading, a quasi-elastic zone is observed, the stress is linear with the deformation, and in all samples, there are no AE signals exceeding the threshold value of the acoustic filter of 40 dB, which indicates a low intensity of internal destruction. The quasi-elastic deformation zone is of the greatest engineering interest, since under elastic stresses, the parts retain their mechanical properties. In the elastic zone, the Young's Modulus was determined by the tangent to the strain–stress curve (Figure 5). The calculated Young's Modulus in quasi-elastic zones and maximum strength for samples are shown in the graphs (Figure 6).

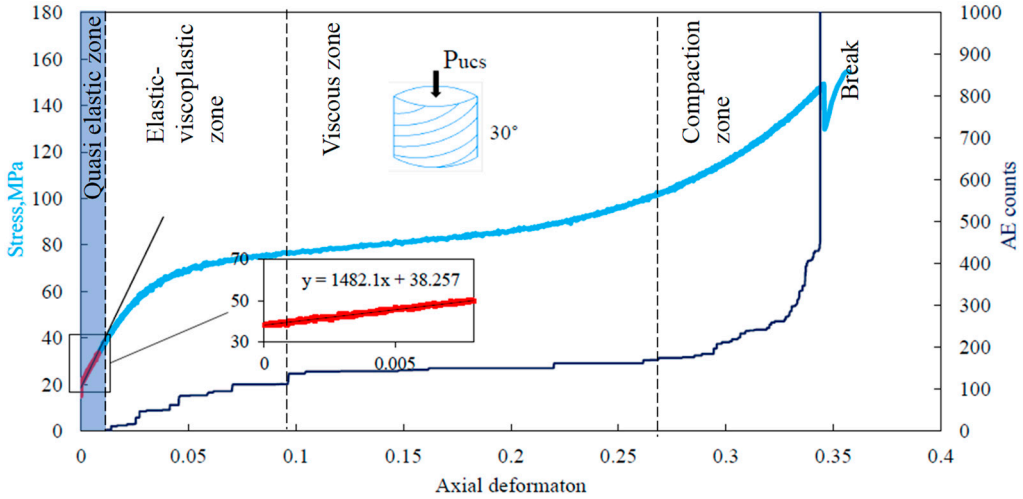

Figure 5. Typical stress–strain curve and total AE signal curve for a sample with a layer angle of 30°. Light blue line—stress; dark blue line—total number of AE signals. Vertical dotted lines—boundaries of deformation types. The zone with quasi-elastic deformation is highlighted in blue. The tangent black line is used to determine Young's modulus.

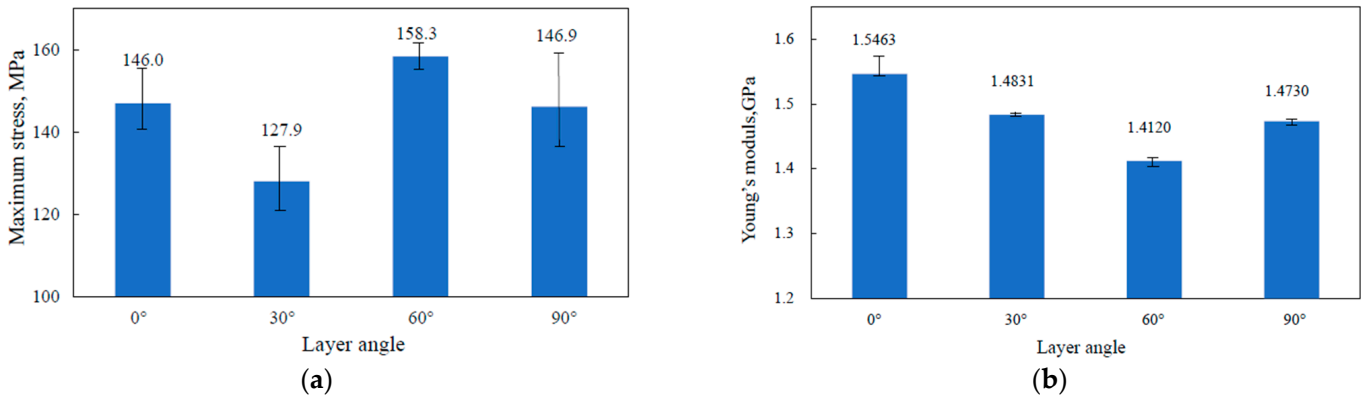

Figure 6. Measured maximum strength (**a**) and Young's modulus under quasi-elastic loading (**b**).

The uniaxial compression test data revealed that samples with layers 60° to the load vector exhibited the highest strength, while those with 30° layers displayed the lowest strength (Figure 7a). Samples with layers parallel and perpendicular to the load vector demonstrated comparable strength. Analysis of Young's modulus indicated that samples with parallel layers exhibited the highest values, while those with 60° layers showed the lowest. Figure 7b illustrates a general trend of decreasing Young's modulus with increasing layer angle relative to the load vector. However, the Young's modulus of samples with perpendicular layers was comparable to that of those with 30°. The disparity in the ratio between maximum uniaxial compression stress and Young's modulus suggests distinct failure mechanisms across the samples. Samples oriented at 0° and 30° to the load vector exhibited the lowest strength, yet displayed high Young's modulus under quasi-elastic stresses, indicating high rigidity and low ductility. In contrast, the sample with a 60° inclination exhibited the highest maximum stress, but lower rigidity under elastic loading.

Based on data acquired from strain sensors adhered to the side surfaces of the samples, axial and radial strain graphs under quasi-elastic loading were constructed (Figure 6). All stress–strain curves exhibited linear behavior. Analysis revealed a consistent influence of sensor location relative to the print axes on the slope of the stress–strain curves across all samples. In samples with inclined and vertical layers, the observed discrepancies in radial strains are likely attributable to interlayer sliding. Surprisingly, the sample featuring layers perpendicular to the cylinder axis also exhibited a dependence of strain on print orientation, suggesting heterogeneity within the print layers along the plane. This observation is likely a consequence of the unique characteristics of LCD printing.

The calculated Poisson's ratios for samples with varying layer angles and printing orientations are presented in Figure 8. The graph reveals that under quasi-elastic loading, samples with layers parallel to the load vector exhibit the lowest Poisson's ratio, while those with a 30° inclination angle to the load vector display the highest. A positive correlation exists between increasing layer inclination angle and decreasing Poisson's ratio. Notably, some calculated Poisson's ratios exceed 0.5, suggesting potential volume changes due to internal microdestruction. The influence of sample orientation relative to the printing plane on Poisson's ratio is also evident (Figure 1). Along the Y-axis, all samples exhibit a 40–60% higher calculated Poisson's ratio compared to the X-axis. The most significant difference in X-Y radial deformations (60%) is observed in samples printed at a 90° angle to the cylinder axis. Figure 8b illustrates the relationship between radial strain gauge orientation and Poisson's ratio variations. Under uniaxial compression, a complex stress–strain state develops within the sample, characterized by maximum tensile stresses at the sample's center. The discrepancy in calculated Poisson's ratios suggests that sample expansion is likely due to crack formation, preferentially oriented along the printer's X-axis.

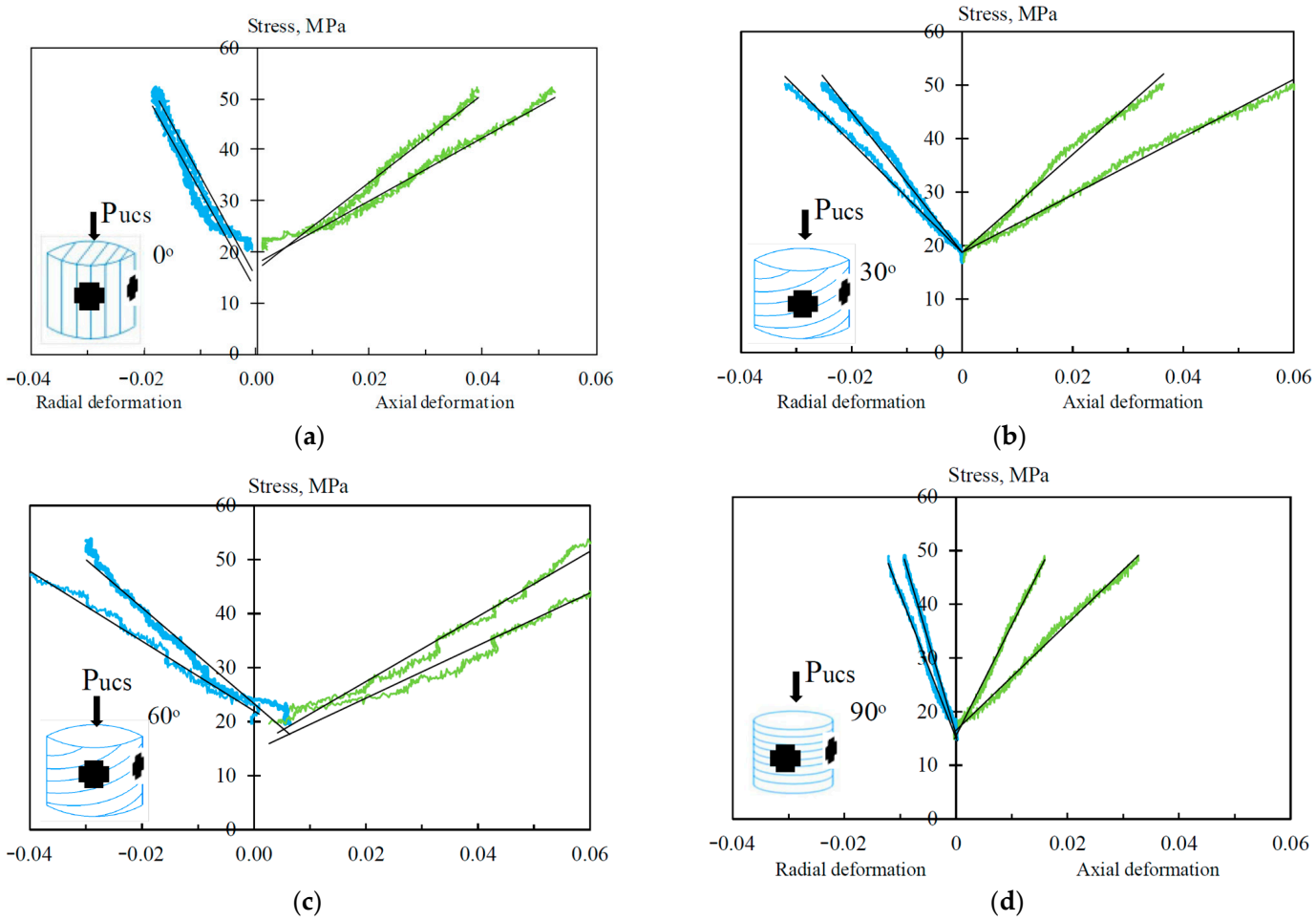

Figure 7. Stress–strain curve for samples—0° (**a**), 30° (**b**), 60° (**c**), and 90° (**d**). Light blue lines—axial strains; green—radial. The graphs schematically show the images with strain gauges and the angle of inclination of the layers relative to the strain vector.

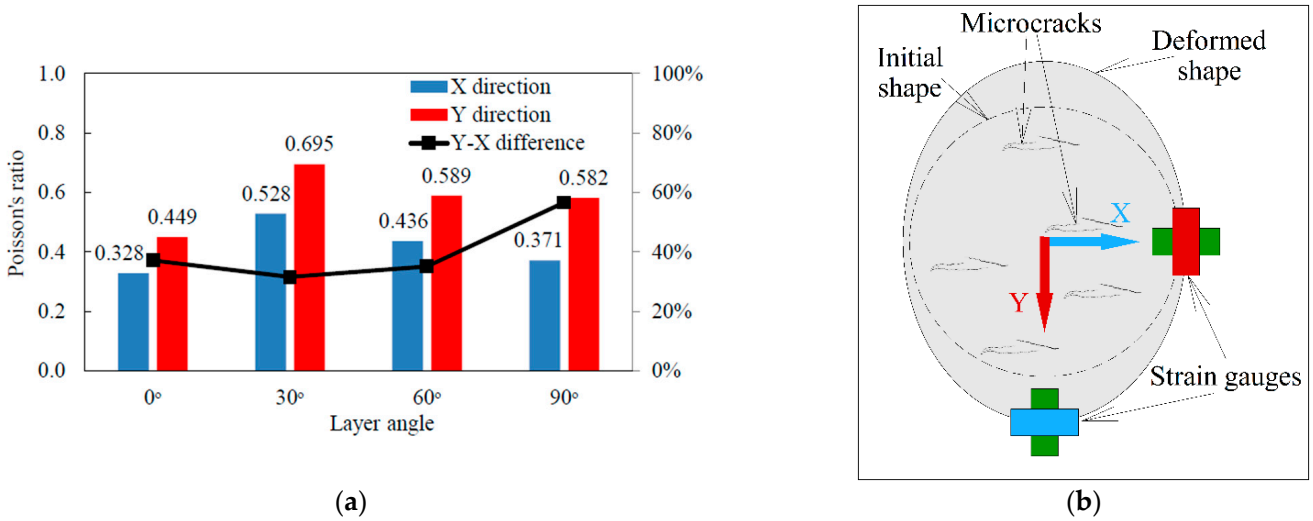

Figure 8. Calculated Poisson's ratios for samples with different print orientations (**a**). Schematic representation of sample deformations relative to the orientation along the print axes (**b**). The color of the sensors corresponds to the direction of the print axis along which the deformation is measured: blue—X-axis; red—Y; green—Z (see Figure 1).

This study uniquely distinguishes itself from prior research on the influence of printing angle on SLA-printed material strength by concurrently measuring the number of

acoustic emission (AE) signals during sample loading (Figure 9). Analyzing the total AE signal count provides a deeper understanding of the failure mechanism, and elucidates the connection between the plastic–brittle transition during deformation within this heterogeneous material.

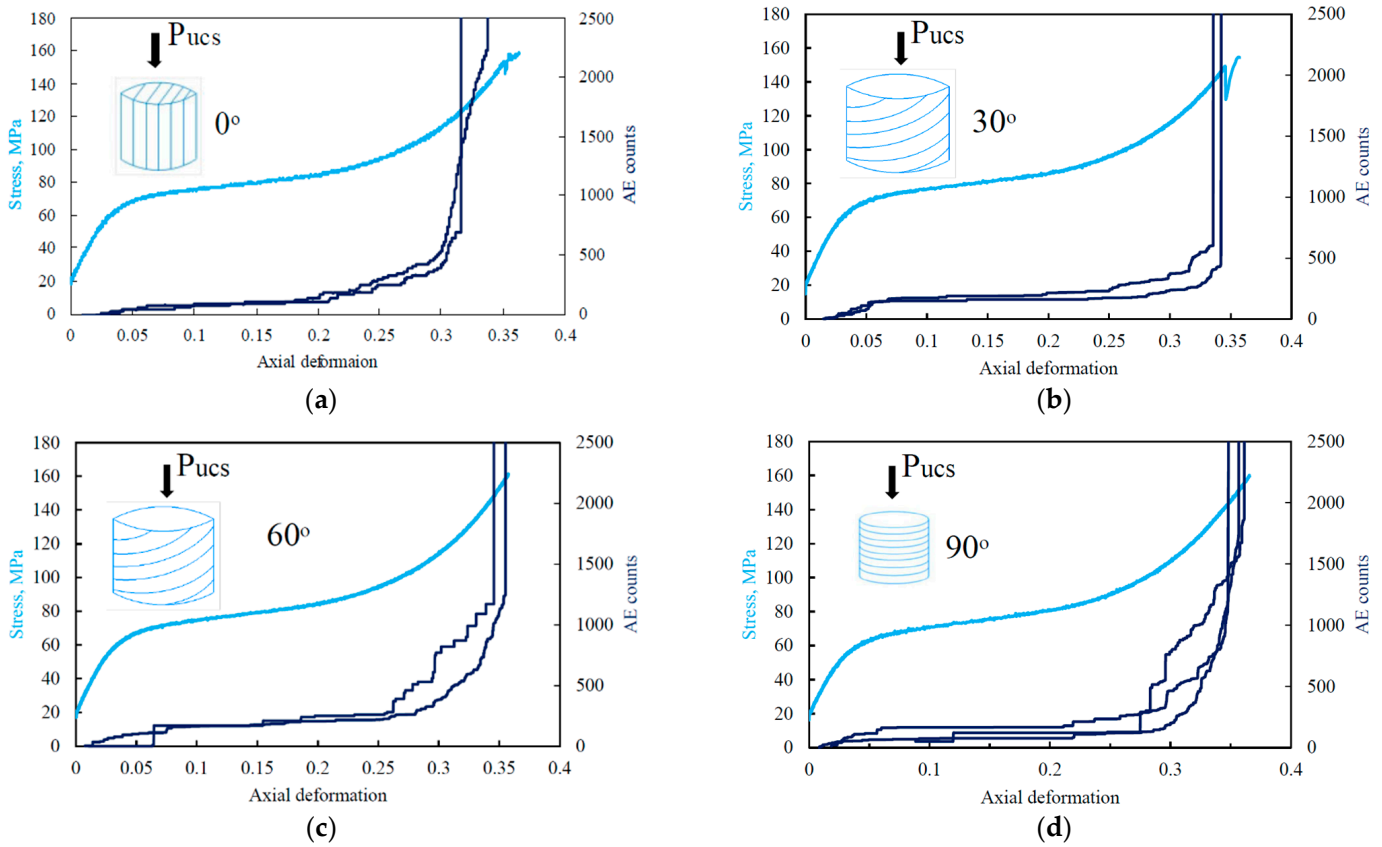

Figure 9. Total number of AE signals for samples—0° (**a**), 30° (**b**), 60° (**c**), and 90° (**d**). Light blue line—stress; dark blue lines—total number of AE signals.

Samples produced using 3D SLA technology exhibit a layered heterogeneity, potentially leading to varied acoustic activity under applied stress. Once the stress surpasses the quasi-elastic deformation limit, plastic deformations (elastic-viscoplastic zone) initiate within the material, accompanied by a significant increase in AE signals (Figure 9). Notably, the onset of AE signals after the quasi-elastic zone occurs at roughly the same deformation value (~0.25) for all samples (Figure 9), indicating internal brittle microdestruction within the material. The duration of the microdestruction varies across samples, influenced by the relative orientation of the load vector to the layered structure. Consequently, some layers primarily exhibit tensile cracks, while others exhibit shear cracks.

The elastic-viscoplastic zone concludes earlier in samples with a layer inclination angle of 30° to the loading axis. Samples with layers parallel to the load vector exhibit the lowest overall AE signal count within the elastic-viscoplastic zone. Conversely, the elastic-viscoplastic zone persists longest in samples with perpendicular layers.

Upon reaching a critical density of microcracks, the material transitions to a viscous flow regime, characterized by a period of "quiet creep". This behavior is observed in nearly all samples at a stress level of approximately 70 to 90 MPa. During this flow zone, a significant deformation range of 0.05 to 0.25 occurs with minimal stress increase. Concurrently, acoustic emission (AE) intensity remains low, and the corresponding AE signal curve exhibits negligible changes.

The duration of the flow zone varies significantly depending on the inclination angle of the material layers relative to the load vector. Samples with a 30° inclination angle demonstrate the most prolonged flow zone (Figure 9b). Conversely, samples with layers parallel to the load vector exhibit the shortest flow zone. Notably, samples with inclination angles of 60° and 90° display comparable flow zone durations, ranging from 0.08 to 0.25 of deformation values.

Following the cessation of yield potential, the material undergoes hardening, accompanied by an increase in stress at a constant loading rate. This phase is characterized by an exponential surge in acoustic emission (AE) signals within the compaction zone, signifying internal restructuring and significant material degradation.

Samples with layers of 60° and 90° displayed the most pronounced increase in AE signal counts during relatively minor deformations. These increases were 4 and 7 times greater, respectively, compared to the flow zone. Notably, samples with layers parallel to the load vector also exhibited compaction, evidenced by an increase in AE signals (Figure 9a). However, samples with a 30° layer inclination angle demonstrated minimal acoustic activity during compaction.

Upon completion of the compaction phase, all samples experienced an abrupt surge in AE signals, culminating in sample failure. While samples with layers parallel to the load vector showed a gradual increase in AE signal intensity prior to failure, the remaining samples exhibited a sudden spike in acoustic activity coinciding with material rupture.

Comparative analysis of AE data and uniaxial compression results revealed that, despite exhibiting similar strain–load curves, the failure mechanisms of samples with varying layer inclination angles relative to the loading vector differed. The dynamic pattern of AE signals as a function of deformation (Figure 9) remained consistent across samples with the same printing angle, highlighting the high reproducibility of the experimental results, likely attributed to the standardized post-processing procedure.

The LCD printing process is illustrated schematically in Figure 10a. Curing of the resin is achieved by exposing a thin layer of curable resin to ultraviolet (UV) light emitted from diodes. This UV light is directed between the LCD display and the previously printed layer, which is fixed to a movable plate. The LCD panel's transparent pixels allow the UV light to pass through, while the opaque pixels define the shape of the curable layer (Figure 10f). Due to the square-shaped pixels and their separation by partitions, a pixelation effect is observed on the lower surface of the printed layer (Figure 10a,c,d). The uneven distribution of UV light within the LCD panel leads to further complexities. Along the X-axis, the illuminated rows exhibit an irregular shape, while along the Y-axis, gaps exist between pixel rows (Figure 10f). This uneven irradiation results in a wavy structure with varying degrees of resin polymerization within the layer (Figure 10a). The variable thickness of the cured resin layer contributes to the formation of contraction voids between the display and the cured resin [21], exacerbating the pixelation effect on the lower surface (Figure 10c,d). Additionally, a ribbed surface is formed on the top of the layer in the free volume of the resin (Figure 10e). Through-irradiation results in a decrease in irradiation intensity with distance from the light source due to partial absorption by the resin closer to the screen (Figure 10a,b). This variation in UV intensity leads to layers with uneven strength across the thickness [11,12], with a more cured resin layer closer to the light source (Figure 10a,e). The difference in polymerization across the layer is visually evident in the smoothness of the cleavage surface (Figure 11a). Research by Quagliato et al. [20] found that samples with a low degree of polymerization exhibit smoother crack surfaces, while prolonged polymerization leads to uneven cracks upon rupture.

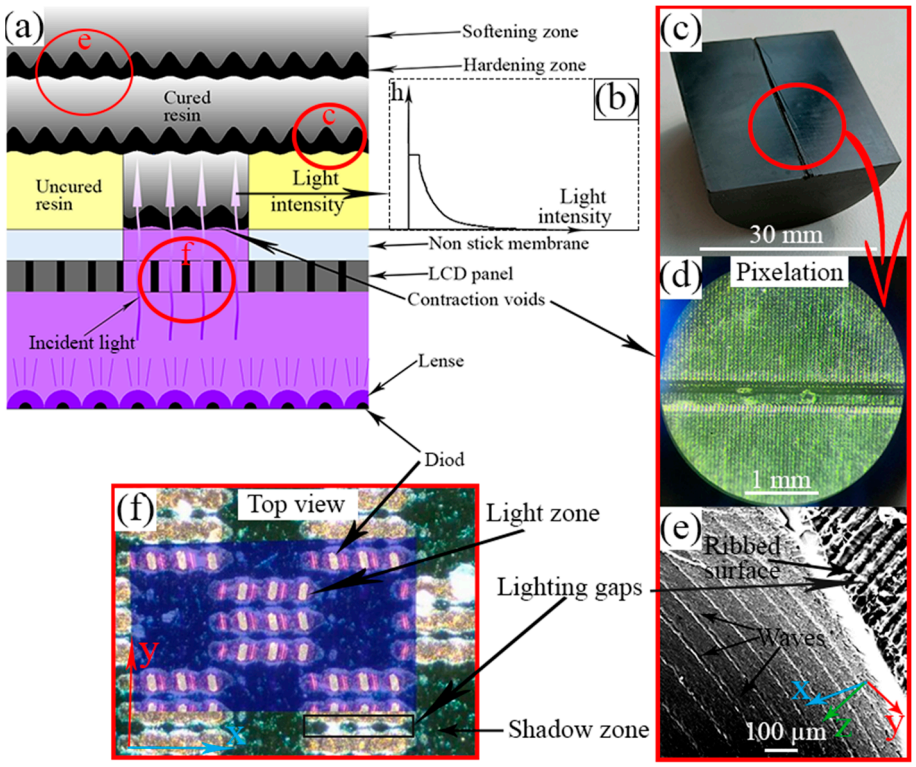

Figure 10. Schematic representation of the influence of printing features on the heterogeneity of samples. (**a**)—layer-by-layer printing; (**b**)—UV intensity; (**c**)—model surface; (**d**)—enlarged surface image; (**e**)—microstructure of the layer and chip surface; (**f**)—display light.

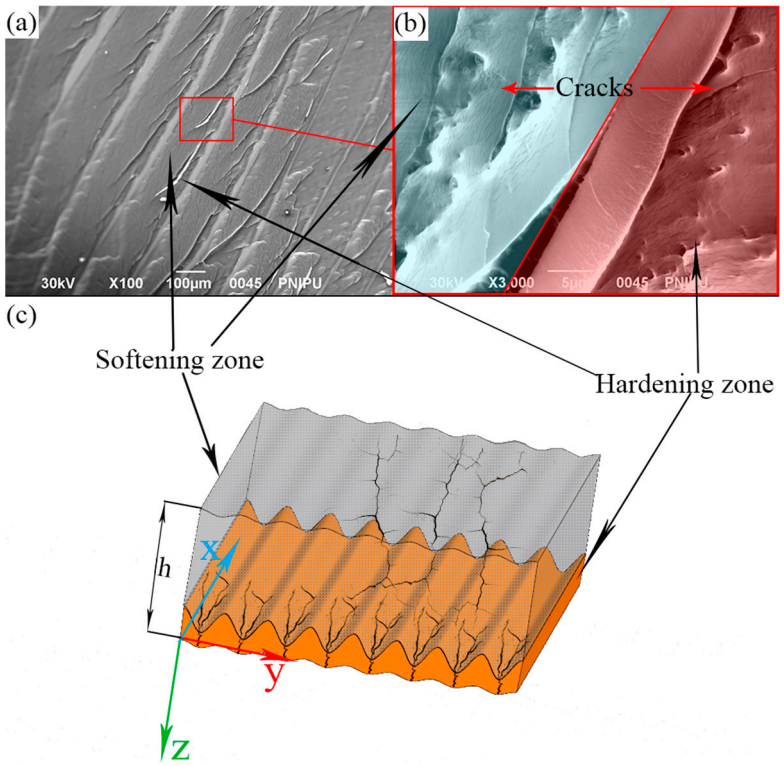

Figure 11. Photo of cleavage of a 3D-printed sample (**a**), showing the heterogeneity of the layers in thickness; (**b**)—enlarged image of the boundary of resin with different degrees of polymerization; (**c**)—schematic representation of the layer and its destruction.

The uneven curing of the resin within the LCD panel, primarily along the Z and Y printing axes, is attributable to the listed features of the panel. This uneven curing results in a layered structure, as evident in Figure 11a, which depicts a chip of the printed material. Closer examination under higher magnification (Figure 11a,b) reveals distinct cracking patterns in layers with varying degrees of polymerization. In the softening zone, cracks primarily propagate along the layer (shear), while in the hardening zone, they are predominantly perpendicular to the layer (rupture). Conceptually, each layer can be envisioned as comprising multiple interlayers (Figure 11c). The lower portion of the layer, closer to the LCD, exhibits greater strength compared to the upper portion and resembles the structure of corrugated chips. Conversely, the softening portion of the layer is characterized by low strength, contributing minimally to the overall material strength. However, its presence induces significant deformations and ductile behavior under shear stresses. The rigidity of the samples, on the other hand, is attributed to the presence of zones with higher polymerization. This layered structure, therefore, governs the deformation and mechanical behavior of the tested samples, influencing their response depending on the orientation relative to the printing axes and the direction of the applied load vector.

In samples with a layer inclination angle of 0°, subjected to uniaxial compression, the load vector is aligned with the X-axis of the print (Figure 11c). The compressive force is primarily perceived by the hardening part of the layers, resulting in a higher rigidity and Young's modulus (Figure 6b). Due to the vertical arrangement of the layers, the material exhibits the lowest flow rate among all tested samples. Under high loads corresponding to the compaction zone (Figure 9a), failure occurs through layer splitting, primarily along the softening part of the layers. This failure mode is characterized by a weak, linearly increasing intensity of acoustic emission signals. Visually, the samples exhibit uniform failure without significant distortions, resulting in longitudinal fragments (Figure 12a). Rupture cracks along the layers are clearly visible at the ends of the failed sample. The cracks on the end demonstrate a preferred direction, with the primary crack traversing the sample along the Z-axis of the print (Figure 12a).

In samples with a 30° layer orientation subjected to uniaxial compression, shear forces develop parallel to the layer plane. This shear force promotes deformation and failure primarily along the softening regions of the layers, as evidenced by the low acoustic emission signal intensity throughout the test (Figure 9b). These samples also exhibit the lowest compressive strength (Figure 6a) and the highest Poisson's ratios in both directions relative to the print, indicating early failure under quasi-elastic loading. The alignment of the layer inclination angle with the shear force results in the sample fracturing into large pieces with minimal fragmentation during failure (Figure 12b). The sample ends show uneven cracking, with diagonal end zones exhibiting wear caused by friction against the press plates (Figure 12b). This is characteristic of layers in contact with both the upper and lower loading cell plates. On the remaining larger portion of the end, friction wear is less pronounced. However, the ends of individual samples exhibit different cracking patterns, suggesting a lack of connection between these layers.

In samples exhibiting a layer angle of 60°, subjected to uniaxial compression, the vertical load is predominantly borne by the weaker, shear-prone components of the layers. This arrangement leads to increased total slip due to the numerous inclined layers along the cylinder axis, resulting in the greatest longitudinal deformation (Figure 7c) and the lowest Young's modulus (Figure 6b). Acoustic emission analysis revealed that these samples exhibit the longest compaction period under loading (Figure 9c), which ultimately contributes to enhanced material strength (Figure 6a). Due to the inclined arrangement of the layers, the growth of vertical rupture cracks is limited; the ends of the samples with a layer angle of 60° have fewer failures compared to the other samples. Additionally,

the sliding of the printing layers leads to uneven failure of the sample along the Y-axis (Figure 12c).

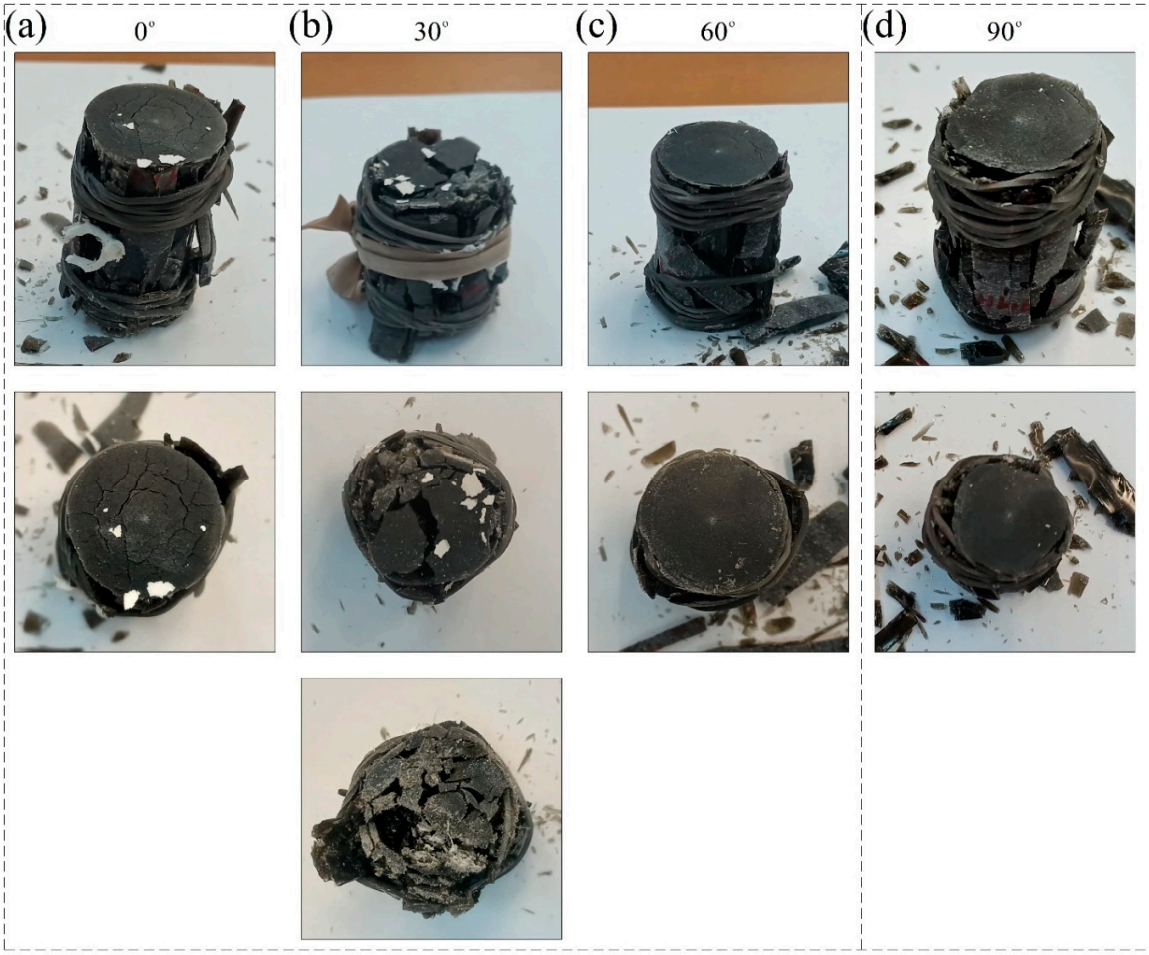

Figure 12. Specimens after uniaxial compression. Layer inclination angle—0° (**a**), 30° (**b**), 60° (**c**), and 90° (**d**).

In samples with 90° layers, the hardening portion of the layer exhibits less compression under load compared to samples with other layer orientations. This hardening portion effectively absorbs tensile forces applied in the middle of the sample, mitigating excessive elongation of the softened portion along the layer. A distinctive characteristic of these samples is the significant anisotropy in Poisson's ratios observed relative to the X-Y printer axes (Figure 8a). This anisotropy can be attributed to the corrugated chip structure, where the thinned portion of the layer acts as stress concentrators. Under pure tensile loading, layer rupture occurs preferentially in the thin regions along the Y-axis (Figure 11c). Conversely, in samples with perpendicular layers within the compaction zone, the acoustic emission (AE) intensity is maximized due to the absence of pre-existing shear deformation within the layers and the subsequent failure of the stronger interlayers. No main cracks are observed at the sample ends (Figure 12d) as the perpendicular layers effectively obstruct the propagation of vertical cracks.

The microstructure of the 3D-printed samples was examined using scanning electron microscopy (SEM). Figures 13 and 14 present SEM micrographs of the chips at varying magnifications. Figure 13 compares the morphology of chips printed along the X and Y axes. The micrographs clearly reveal a layered, heterogeneous structure within the samples. Thin layers enriched with a higher degree of polymerization are evident, particularly near the LCD display where UV irradiation intensity is highest. Chips of samples printed along

the Y-axis exhibit a distinct wavy boundary at the upper edge of the hardened layer. This is attributed to the printing features described previously. Additionally, the hardened layers along the X-axis display an alternating thickness pattern (Figure 13b). This variation is likely a consequence of a crack intersecting the layers at an oblique angle.

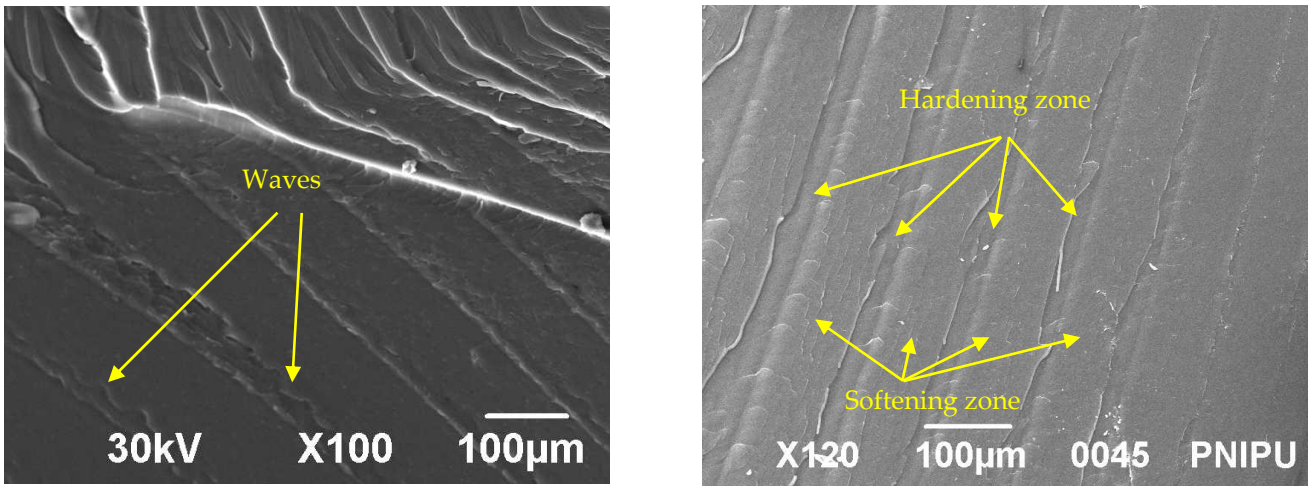

(**a**) (**b**)

Figure 13. Micrographs of the crack surface in the sample: (**a**) along the Y-axis; (**b**) along the X-axis.

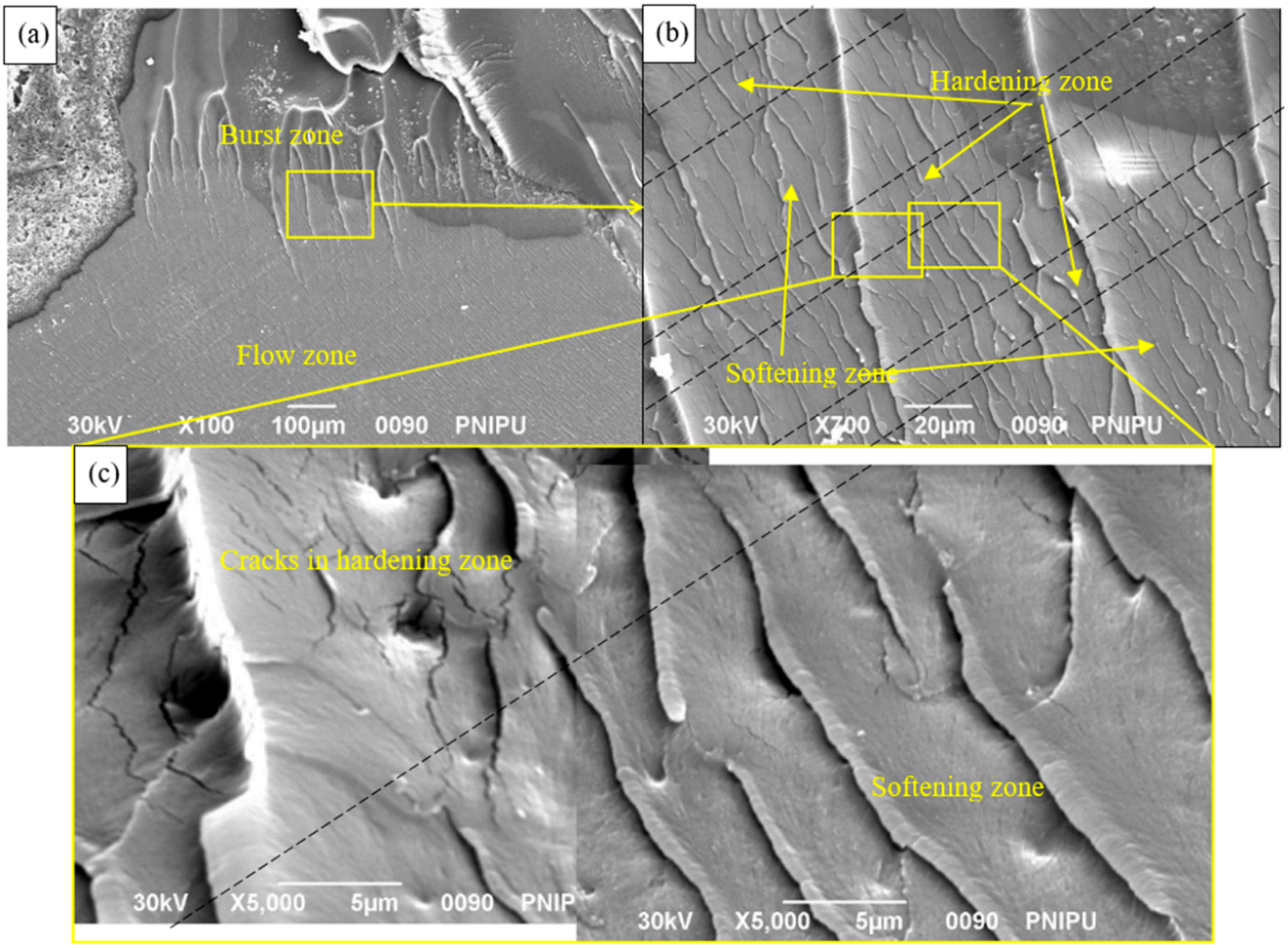

Figure 14. Micrographs of the crack surface of the sample in the flow zone, at magnifications of (**a**) 100×, (**b**) 700×, and (**c**) 5000×.

The micrographs in Figure 14 show the transition between the flow and rupture zones of the crack, which propagates along the printer's X-axis. The image highlights the layered structure of the samples. A closer examination (Figure 14b) reveals that during rupture, small ribs originating from the flow zone gradually coalesce into larger faces, ultimately transitioning into the rupture zone. At a magnification of 5000× (Figure 14c), the hardening zone exhibits numerous microcracks, while no cracks are observed in the softening layer. This observation can be attributed to the higher brittleness of layers with a high degree of polymerization, while the softer layers exhibit dactylicity. Consequently, the analysis of the crack microstructure supports previous conclusions regarding the influence of layer inclination angle and print orientation along the printer axes on the mechanical properties of 3D-printed samples.

4. Conclusions

The experimental studies investigating the effect of layer inclination angle on the mechanical properties of 3D SLA-printed samples under uniaxial compression yielded the following conclusions:

1. Post-processing of printed samples in accordance with ASTM D7012-23 ensured a high degree of convergence of test results for samples with the same layer inclination angles.
2. The uniaxial compression test data revealed that samples with an inclined layer orientation at 60° to the load vector exhibited the highest strength. Conversely, samples with a 30° inclination displayed the lowest strength. Samples with layer orientations parallel and perpendicular to the load vector demonstrated equivalent strength.
3. This study revealed that specimens with parallel layers to the load vector exhibited the highest Young's modulus. Conversely, specimens with an angle of 60° to the load vector displayed the lowest Young's modulus. Variations in the ratio between maximum stress during uniaxial compression and Young's modulus indicated distinct failure mechanisms among the specimens. Notably, samples oriented at 0° and 30° to the load vector demonstrated different strength, accompanied by a relatively high equal modulus of elasticity under quasi-elastic stress conditions. These specimens exhibited high rigidity, but concurrently possessed low ductility.
4. Under quasi-elastic loading conditions, the Poisson's ratio exhibited a strong dependence on sample orientation. Samples with layers parallel to the load vector displayed the lowest Poisson's ratio, while those inclined at 30° to the load vector exhibited the highest. Furthermore, a significant anisotropy in Poisson's ratio was observed relative to the printing plane. Samples consistently exhibited a 40–60% higher Poisson's ratio along the Y-axis compared to the X-axis. This anisotropy was most pronounced in samples printed at a 90° angle to the cylinder axis, where the difference in radial deformations between the X and Y directions reached 60%. The observed variation in Poisson's ratios suggests that the expansion of the samples under load is influenced by the formation of cracks, which preferentially align along the X-axis of the printer.
5. A comparative analysis of acoustic emission (AE) data and uniaxial compression results revealed that, despite exhibiting similar strain–load curves, samples with varying layer inclination angles relative to the loading vector displayed distinct failure mechanisms. The dynamics of AE signal counts during deformation for samples with identical printing angles were consistent, suggesting a high degree of convergence in the experimental results, likely attributed to the post-processing procedure applied to the samples.
6. A detailed analysis of the crack surfaces in 3D-printed samples revealed a layered, heterogeneous microstructure. This heterogeneity arises from varying degrees of resin

polymerization within each layer, a consequence of the inherent characteristics of the LCD printing process. Uneven UV irradiation during printing results in non-uniform curing of the resin, particularly along the printer axes Z and Y. Examination of crack surfaces along the Y-Z plane revealed a distinct wavy boundary within each layer, separating regions of varying polymerization. The "softening" regions exhibit lower polymerization and, consequently, reduced strength, contributing minimally to the overall sample strength. However, their presence promotes significant deformations and ductile behavior under shear stresses. Conversely, the rigidity of the samples is attributed to zones of higher polymerization within the layers. This layered structure, characterized by varying degrees of polymerization, results in anisotropic deformation and mechanical behavior of the printed samples. The orientation relative to the printing axes and the direction of the load vector significantly influence the sample's response to stress.

This research addresses a critical gap in the understanding of how layer orientation in 3D printing influences the strength properties of components under uniaxial compression. Through comprehensive analysis, this study elucidates the failure mechanism and provides insights into the varying strength observed across different printing layer angles. The findings have significant implications for the design and production of components using 3D SLA printing, enabling more efficient utilization of such components under compressive loads.

Author Contributions: Conceptualization, methodology, E.K.; software, A.P.; validation, M.T.; formal analysis, E.R.; investigation, A.G., A.P., Y.S. and Z.I.; resources, E.K.; data curation, E.K.; writing—original draft preparation, E.K.; writing—review and editing, E.K.; visualization, E.R. and Z.I.; supervision, E.K.; project administration, E.K. All authors have read and agreed to the published version of the manuscript.

Funding: This research was funded by the Ministry of science and higher education of the Russian Federation (Project № FSNM-2024-0008).

Data Availability Statement: The datasets analyzed during the current study are available from the corresponding author on reasonable request.

Conflicts of Interest: The authors declare no conflicts of interest.

References

1. Johnson, P.R.; Copeland, P.M.; Ayodele, A.O.; Tarekegn, E.N.; Bromley, S.J.; Harrell, W.R.; Sosolik, C.E.; Marler, J.P. In-vacuum performance of a 3D-printed ion deflector. *Vacuum* **2020**, *172*, 109061. [CrossRef]
2. AL-Hasni, S.; Santori, G. 3D printing of vacuum and pressure tight polymer vessels for thermally driven chillers and heat pumps. *Vacuum* **2020**, *171*, 109017. [CrossRef]
3. Dong, D.; Su, H.; Li, X.; Fan, G.; Zhao, D.; Shen, Z.; Liu, Y.; Guo, Y.; Yang, C.; Liu, L.; et al. Microstructures and mechanical properties of biphasic calcium phosphate bioceramics fabricated by SLA 3D printing. *J. Manuf. Process* **2022**, *81*, 433–443. [CrossRef]
4. Cheng, P.; Wang, K.; Peng, Y.; Ahzi, S.; Xu, F.; Huang, Z. A novel 3D printed continuous ramie fiber reinforced variable stiffness biocomposite honeycomb structure. *Vacuum* **2023**, *215*, 112301. [CrossRef]
5. Sotov, A.; Kantyukov, A.; Popovich, A.; Sufiiarov, V. LCD-SLA 3D printing of BaTiO3 piezoelectric ceramics. *Ceram. Int.* **2021**, *47*, 30358–30366. [CrossRef]
6. Dulieu-Barton, J.M.; Fulton, M.C. Mechanical Properties of a Typical Stereolithography Resin. *Strain* **2000**, *36*, 81–87. [CrossRef]
7. Puebla, K.; Arcaute, K.; Quintana, R.; Wicker, R.B. Effects of environmental conditions, aging, and build orientations on the mechanical properties of ASTM type I specimens manufactured via stereolithography. *Rapid Prototyp. J.* **2012**, *18*, 374–388. [CrossRef]
8. Chen, Q.; Zou, B.; Lai, Q.; Zhao, Y.; Zhu, K. Influence of irradiation parameters on the curing and interfacial tensile strength of HAP printed part fabricated by SLA-3D printing. *J. Eur. Ceram. Soc.* **2022**, *42*, 6721–6732. [CrossRef]

9. Rehbein, T.; Johlitz, M.; Lion, A.; Sekmen, K.; Constantinescu, A. Temperature- and degree of cure-dependent viscoelastic properties of photopolymer resins used in digital light processing. *Progress. Addit. Manuf.* **2021**, *6*, 743–756. [CrossRef]
10. Shirinbayan, M.; Zirak, N.; Saddaoui, O.; Mammeri, A.; Azzouz, K.; Benfriha, K.; Tcharkhtchi, A.; Fitoussi, J. Effect of build orientation and post-curing of (meth)acrylate-based photocurable resin fabricated by stereolithography on the mechanical behavior from quasi-static to high strain rate loadings. *Int. J. Adv. Manuf. Technol.* **2022**, *123*, 1877–1887. [CrossRef]
11. Lee, J.H.; Prud'homme, R.K.; Aksay, I.A. Cure depth in photopolymerization: Experiments and theory. *J. Mater. Res.* **2001**, *16*, 3536–3544. [CrossRef]
12. Lee, E.-D.; Sim, J.-H.; Kweon, H.-J.; Paik, I.-H. Determination of process parameters in stereolithography using neural network. *KSME Int. J.* **2004**, *18*, 443–452. [CrossRef]
13. Li, Y.; Teng, Z. Effect of printing orientation on mechanical properties of SLA 3D-printed photopolymer. *Fatigue Fract. Eng. Mater. Struct.* **2024**, *47*, 1531–1545. [CrossRef]
14. Monzón, M.; Ortega, Z.; Hernández, A.; Paz, R.; Ortega, F. Anisotropy of Photopolymer Parts Made by Digital Light Processing. *Materials* **2017**, *10*, 64. [CrossRef]
15. Saini, J.; Dowling, L.; Kennedy, J.; Trimble, D. Investigations of the mechanical properties on different print orientations in SLA 3D printed resin. *Proc. Inst. Mech. Eng. C J. Mech. Eng. Sci.* **2020**, *234*, 2279–2293. [CrossRef]
16. Farkas, A.Z.; Galatanu, S.-V.; Nagib, R. The Influence of Printing Layer Thickness and Orientation on the Mechanical Properties of DLP 3D-Printed Dental Resin. *Polymers* **2023**, *15*, 1113. [CrossRef]
17. Keßler, A.; Hickel, R.; Ilie, N. In vitro investigation of the influence of printing direction on the flexural strength, flexural modulus and fractographic analysis of 3D-printed temporary materials. *Dent. Mater. J.* **2021**, *40*, 641–649. [CrossRef]
18. Cosmi, F.; Maso, A.D. A mechanical characterization of SLA 3D-printed specimens for low-budget applications. *Mater. Today Proc.* **2020**, *32*, 194–201. [CrossRef]
19. Pandzic, A. Influence of Layer Height, Build Orientation and Post Curing on Tensile Mechanical Properties of SLA 3D Printed Material. In Proceedings of the 32nd DAAAM International Symposium on Intelligent Manufacturing and Automation, Vienna, Austria, 25–31 October 2021; pp. 200–208. [CrossRef]
20. Quagliato, L.; Kim, S.Y.; Ryu, S.C. Quasi-ductile to brittle transitional behavior and material properties gradient for additively manufactured SLA acrylate. *Mater. Lett.* **2022**, *329*, 133121. [CrossRef]
21. Mehdikhani, M.; Gorbatikh, L.; Verpoest, I.; Lomov, S.V. Voids in fiber-reinforced polymer composites: A review on their formation, characteristics, and effects on mechanical performance. *J. Compos. Mater.* **2019**, *53*, 1579–1669. [CrossRef]